NUMERICAL MODELING OF THE GLOBAL TSUNAMI:

Indonesian Tsunami of 26 December 2004

Zygmunt Kowalik, Institute of Marine Science, University of Alaska
William Knight, NOAA/NWS/West Coast and Alaska Tsunami Warning Center
Tom Logan, Arctic Region Supercomputing Center
Paul Whitmore, NOAA/NWS/West Coast and Alaska Tsunami Warning Center

ABSTRACT

A new model for the global tsunami computation is constructed. It includes a high order of approximation for the spatial derivatives. The boundary condition at the shore line is controlled by the total depth and can be set either to runup or to the zero normal velocity. This model, with spatial resolution of one minute, is applied to the tsunami of 26 December 2004 in the World Ocean from 80°S to 69°N. Because the computational domain includes close to 200 million grid points, a parallel version of the code was developed and run on a supercomputer. The high spatial resolution of one minute produces very small numerical dispersion even when tsunamis wave travel over large distances. Model results for the Indonesian tsunami show that the tsunami traveled to every location of the World Ocean. In the Indian Ocean the tsunami properties are related to the source function, i.e., to the magnitude of the bottom displacement and directional properties of the source. In the Southern Ocean surrounding Antarctica, in the Pacific, and especially in the Atlantic, tsunami waves propagate over large distances by energy ducting over oceanic ridges. Tsunami energy is concentrated by long wave trapping over the oceanic ridges. Our computations show the Coriolis force plays a noticeable but secondary role in the trapping. Travel times obtained from computations as arrival of the first significant wave show a clear and consistent pattern only in the region of the high amplitude and in the simply connected domains. The tsunami traveled from Indonesia, around New Zealand, and into the Pacific Ocean. The path through the deep ocean to North America carried miniscule energy, while the stronger signal traveled a much longer distance via South Pacific ridges. The time difference between first signal and later signals strong enough to be recorded at North Pacific locations was several hours.

1. Basic equations and tools

To study tsunami the equations of motion and continuity are formulated in the spherical polar coordinates. λ, ϕ and R, are defined as longitude, latitude and distance from the Earth's center. If the origin of the system is located on the ocean surface, it is more suitable to introduce a vertical coordinate $z = R - R_0$. Here R_0 is the radius of Earth and is equal 6370km.

Because Earth is not exactly spherical, the equations given below will better describe the large scale motion relative to the geopotential and not to the spherical surfaces. For further discussion of this problem see Gill (1982).

The vertically averaged equations of motion and continuity in the spherical system are

$$\frac{\partial u}{\partial t} + \frac{u}{R_\circ \cos\phi}\frac{\partial u}{\partial\lambda} + \frac{v}{R_\circ}\frac{\partial u}{\partial\phi} - (2\Omega + \frac{u}{R_\circ \cos\phi})v\sin\phi =$$

$$-\frac{g}{R_\circ \cos\phi}\frac{\partial\zeta}{\partial\lambda} - \frac{\tau_\lambda^b}{\rho_o D} \tag{1}$$

$$\frac{\partial v}{\partial t} + \frac{u}{R_\circ \cos\phi}\frac{\partial v}{\partial\lambda} + \frac{v}{R_\circ}\frac{\partial v}{\partial\phi} + (2\Omega + \frac{u}{R_\circ \cos\phi})u\sin\phi = -\frac{g}{R_\circ}\frac{\partial\zeta}{\partial\phi} - \frac{\tau_\phi^b}{\rho_o D} \tag{2}$$

$$\frac{\partial\zeta}{\partial t} - \frac{\partial\eta}{\partial t} + \frac{1}{R_\circ \cos\phi}\frac{\partial uD}{\partial\lambda} + \frac{1}{R_\circ \cos\phi}\frac{\partial}{\partial\phi}(Dv\cos\phi) = 0 \tag{3}$$

In the above equations, u is the velocity in the λ (E-W) direction, v denotes the velocity in the ϕ (N-S) direction, and ζ is the sea level, η is the bottom displacement, t is the time, g is Earth's gravity acceleration (g=981 cm s^{-2}), ρ is water density, and D is the total depth $D = H + \zeta - \eta$. The Coriolis parameter will be taken as $f = 2\Omega\sin\phi$. It is a function of the Earth's angular velocity $\Omega = 7.29\times10^{-5}s^{-1}$ and the latitude ϕ. The components of the bottom friction force are nonlinear functions of velocity:

$$\tau_\lambda^b = ru\sqrt{(u^2 + v^2)} \qquad \text{and} \qquad \tau_\phi^b = rv\sqrt{(u^2 + v^2)}$$

To simplify the bottom friction terms in eqs. (1) and (2) the following notation is introduced:

$$\frac{\tau_\lambda^b}{\rho_o D} = \frac{ru\sqrt{(u^2 + v^2)}}{\rho_o D} = R_x u \tag{4a}$$

$$\frac{\tau_\phi^b}{\rho_o D} = \frac{rv\sqrt{(u^2 + v^2)}}{\rho_o D} = R_y v \tag{4b}$$

The dimensionless bottom friction coefficient r is taken as 3.3×10^{-3}.

In order to identify important steps in the construction of a global numerical code we shall jot down basic numerical formulas for the spherical coordinate system. The computation will be done in a space staggered grid (C grid) given in Fig.1. The u velocity grid points denoted as horizontal bars are offset from the v velocity grid points (vertical bars). Sea level grid points are denoted by crosses. The grid size (space step) along the

E-W direction is $h_\lambda = R_\circ \cos\phi \Delta\lambda$. Index $j = 1, \ldots$ stands for the space stepping along the parallels of latitude, thus the distance along the parallels is expressed as jh_λ. As the parallels of latitudes become very small circles near the poles, this geographical region needs to be either excluded from consideration or introduced into computation through a different map projection. In this study, we exclude the poles from the computational domain. The space step along the N-S direction is $h_\phi = R_\circ \Delta\phi$. Index k stands for the space stepping along the meridians of longitude. Locations of the grid points on the sphere are given by their j and k coordinates.
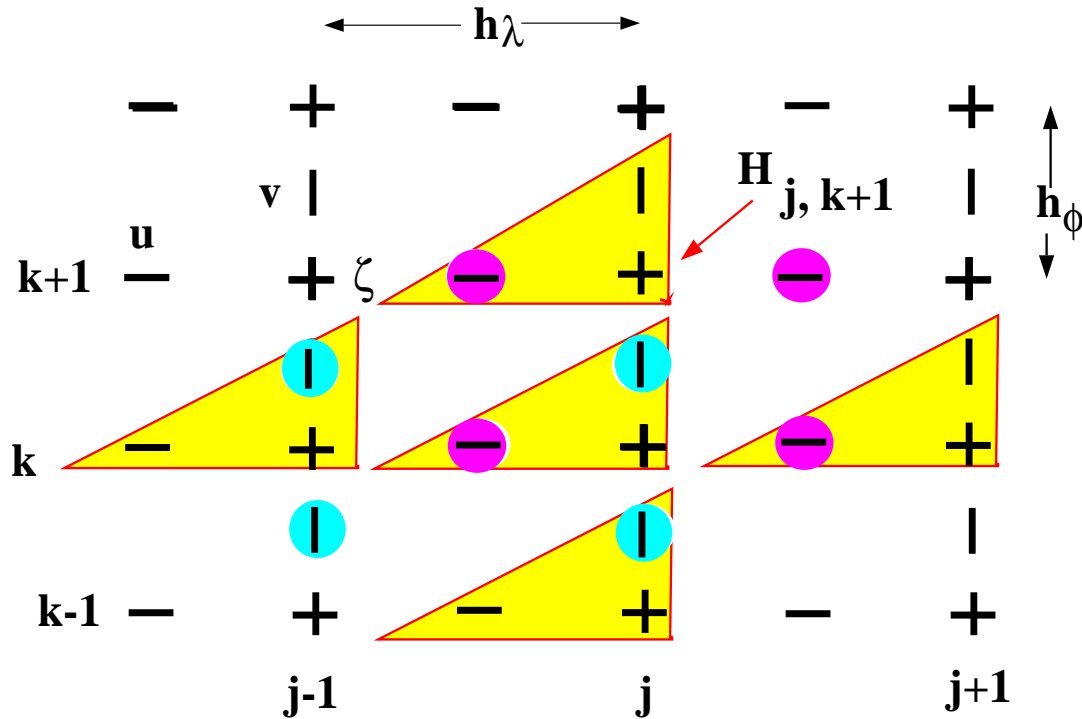

Figure 1
Spatial grid distribution in the spherical system of coordinates.

The u, v and ζ points are organized into triplets as shown by the yellow triangles in Fig.1. The depth is defined at the sea level points. To resolve some terms in the equations of motion the v velocity is needed at the u locations and vice versa. For this reason the blue and red circles are introduced to explain how the averaged values are constructed. The four values given by blue circles, when averaged will define the averaged v velocity at the u point location. This point location is given by $u_{j,k}$. The averaged v velocity at this location is $\bar{v}^u = 0.25(v_{j,k-1} + v_{j,k} + v_{j-1,k} + v_{j-1,k-1})$. In a similar way the average u velocity (four reddish circles) at the $v_{j,k}$ point is $\bar{u}^v = 0.25(u_{j+1,k} + u_{j+1,k+1} + u_{j,k+1} + u_{j,k})$.

The solution of equations(1-3) is usually advanced in time by the two-time-level numerical scheme (Kowalik and Murty, 1993; Imamura, 1996). For the spatial derivatives the second order of approximation is constructed.

$$u_{j,k}^{m+1} = u_{j,k}^m - \frac{gT}{h_\lambda}(\zeta_{j,k}^m - \zeta_{j-1,k}^m) + Tf\bar{v}^{u,m} + \frac{T\tan\phi_k^\zeta}{R_\circ}\bar{v}^{u,m}u_{j,k}^m - TR_{x,j,k}^m u_{j,k}^m$$

$$-\frac{u_p^m T}{h_\lambda}(u_{j,k}^m - u_{j-1,k}^m) - \frac{u_n^m T}{h_\lambda}(u_{j+1}^m - u_j^m)$$

$$-\frac{T\bar{v}_p^{u,m}}{h_\phi}(u_{j,k}^m - u_{j,k-1}^m) - \frac{T\bar{v}_n^{u,m}}{h_\phi}(u_{j,k+1}^m - u_{j,k}^m) \qquad (5)$$

$$v_{j,k}^{m+1} = v_{j,k}^m - \frac{gT}{h_\phi}(\zeta_{j,k+1}^m - \zeta_{j,k}^m) - Tf\bar{u}^{v,m+1} - \frac{T\tan\phi_k^v}{R_\circ}\bar{u}^{v,m}\bar{u}^{v,m+1} - TR_{y,j,k}^m v_{j,k}^m$$

$$-\frac{T\bar{u}_p^{v,m}}{h_\lambda}(v_{j,k}^m - v_{j-1,k}^m) - \frac{T\bar{u}_n^{v,m}}{h_\lambda}(v_{j+1,k}^m - v_{j,k}^m)$$

$$-\frac{Tv_p^m}{h_\phi}(v_{j,k}^m - v_{j,k-1}^m) - \frac{Tv_n^m}{h_\phi}(v_{j,k+1}^m - v_{j,k}^m) \qquad (6)$$

$$\zeta_{j,k}^{m+1} = \zeta_{j,k}^m - \frac{T}{h_\lambda}(flux_{\lambda,j+1,k} - flux_{\lambda,j,k})$$

$$-\frac{T}{cos\phi_k^\zeta h_\phi}(flux_{\phi,j,k} - flux_{\phi,j,k-1}) + \eta_{j,k}^{m+1} - \eta_{j,k}^m \qquad (7)$$

In this numerical approach we aim to construct the high order of approximation in space for the continuity equation. For this purpose we expanded the upwind/downwind flux code proposed by Mader (2004). For the large scale computations the upwind/downwind is essential as it displays strong stability. We have improved the original code by an additional interpolation between the grid points and the resultant code given by eqs. 8 and 9 is close to the third order of approximation in space.

$$flux_{\lambda,j,k} = u_p^{m+1}(\zeta_{p,\lambda}^m - \eta_{j-1,k}^m) + u_n^{m+1}(\zeta_{n,\lambda}^m - \eta_{j,k}^m) + u_{j,k}^{m+1}\frac{(H_{j,k} + H_{j-1,k})}{2} \qquad (8a)$$

$$\zeta_{p,\lambda}^m = (0.5 + u_p^{m+1}\frac{T}{h_\lambda})\zeta_{j-1,k}^m + (0.5 - u_p^{m+1}\frac{T}{h_\lambda})\zeta_{j,k}^m \qquad (8b)$$

$$\zeta_{n,\lambda}^m = (0.5 + u_n^{m+1}\frac{T}{h_\lambda})\zeta_{j-1,k}^m + (0.5 - u_n^{m+1}\frac{T}{h_\lambda})\zeta_{j,k}^m \qquad (8c)$$

$$u_p^{m+1} = 0.5 * (u_{j,k}^{m+1} + |u_{j,k}^{m+1}|) \quad \text{and} \quad u_n^{m+1} = 0.5 * (u_{j,k}^{m+1} - |u_{j,k}^{m+1}|) \qquad (8d)$$

$$flux_{\phi,j,k} = \cos\phi_k^v\left[v_p^{m+1}(\zeta_{p,\phi}^m - \eta_{j,k}^m) + v_n^{m+1}(\zeta_{n,\phi}^m - \eta_{j,k+1}^m) + v_{j,k}^{m+1}\frac{(H_{j,k} + H_{j,k+1})}{2}\right] \qquad (9a)$$

$$\zeta_{p,\phi}^m = (0.5 + v_p^{m+1}\frac{T}{h_\phi})\zeta_{j,k}^m + (0.5 - v_p^{m+1}\frac{T}{h_\phi})\zeta_{j,k+1}^m \qquad (9b)$$

$$\zeta_{n,\phi}^m = (0.5 + v_n^{m+1}\frac{T}{h_\phi})\zeta_{j,k}^m + (0.5 - v_n^{m+1}\frac{T}{h_\phi})\zeta_{j,k+1}^m \qquad (9c)$$

$$v_p^{m+1} = 0.5 * (v_{j,k}^{m+1} + |v_{j,k}^{m+1}|) \quad \text{and} \quad v_n^{m+1} = 0.5 * (v_{j,k}^{m+1} - |v_{j,k}^{m+1}|) \qquad (9d)$$

In the above code the index m stands for the time stepping and the time step is T.

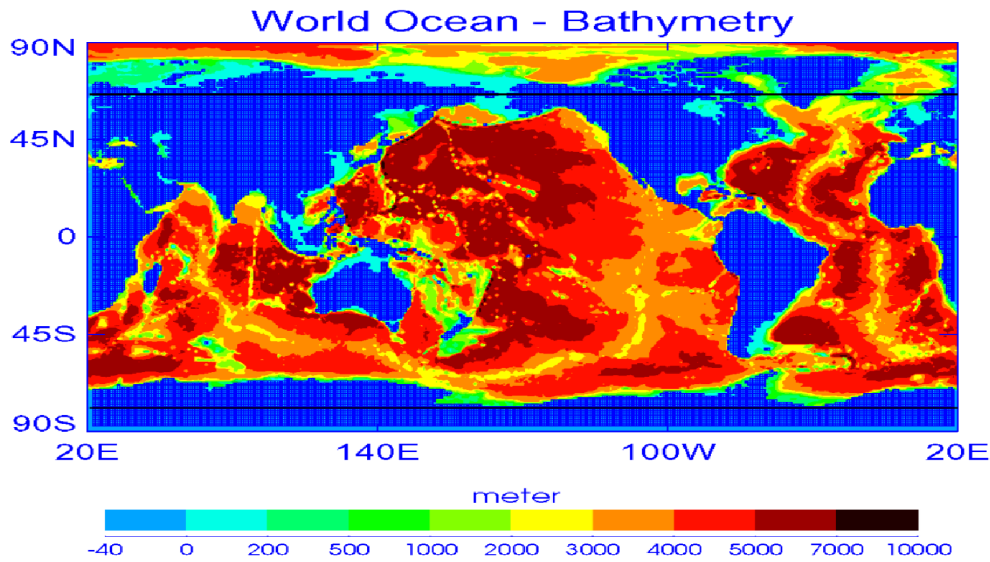## 2. Domain, boundary conditions and numerical grid

Figure 2. Ocean bathymetry. Computational domain extends from 80°S to 69°N.

The integration domain is shown in Fig.2. It extends from 80°S to 69°N. The boundaries include both wet and dry points. Along the coastal (dry points) the normal velocity is set to zero. At the wet boundary points (along 69°N) the radiation condition, established by Reid and Bodine (1968) is used. The entire globe is cut along 20°E longitude, requiring a cyclic boundary condition for sea level and the E-W velocity on this meridian. It appears at the first glance that the above boundary conditions are sufficient to derive a solution. Introductory numerical experiments show that even with the relatively large space step of 1' the new dry and wet points may be generated due to runup or run-down. A numerical scheme for the wetting and drying needs to be introduced.

The total depth $(h + \zeta - \eta)$ is usually taken as the parameter to be tested for the the presence of the wet or dry points (Flather and Heaps (1975) Immamura (1996) and

Kowalik and Murty (1993b)). The wet and dry points are identified by setting the average (undisturbed) ocean depth as positive (wet points) and elevations (dry points) as the negative values. The total depth in the dry grid points is taken as zero $D = h + \zeta = 0$. A simple runup condition is used. The following steps are taken when the dry point $(j_{wet}+1)$ is located to the right of the wet point j_{wet}.

$IF(\zeta^m(j_{wet}) > -H(j_{wet} + 1))$ THEN $u^m_{j_{wet}+1} = u^m_{j_{wet}}$. If wetting is possible (as indicated by the above condition) the velocity from the wet point is extrapolated to the right (dry point), but sea level is calculated through the equation of continuity.

The spatial grid step of numerical computation is $1'$, ($R_0\Delta\phi$=1.852km) and it changes along the circle of longitude as $R_0\Delta\phi\cos\phi$. Numerical stability requires that this step be smaller than distance $T\sqrt{gH}$. The deepest point in the World Ocean (h≃11000m) is located close to 11°N therefore the time step of numerical integration is less than 7.9 s. This step was diminished to 2 s as the runup scheme requires smaller time stepping. The total number of the grid points was close to 2×10^8, therefore the simple time stepping solution, even on a supercomputer may take several weeks. The entire domain was split along the meridians into 40 subdomains to apply 40 processors. With this parallelization, 50hrs of tsunami propagation was reproduced in 9hrs of computer run time.

A small spatial step is important as the short-period waves can be obliterated during large distances of propagation when using large spatial steps. Taking the average depth of the World Ocean as 4000 m, a wave with 10 minute has a wavelength close to 120 km. Such wave length is discretized by the $1'$ grid into about 64 mesh lengths. The amplitude of a sinusoidal wave propagating over distance 10000 km will diminish only about 2%, and some shorter dispersive wave will be generated as well (Kowalik, 2003).

3. Source function

The generation mechanism for the Indian Ocean tsunami is mainly the static sea floor uplift caused by abrupt slip at the India/Burma plate interface. Permanent, vertical sea floor displacement is computed using the static dislocation formulae from Okada (1985). Inputs to these formulae are fault plane location, depth, strike, dip, slip, length, and width as well as seismic moment and rigidity. The earthquake's total rupture extent can be estimated by several approaches. Finite fault seismic data inversion is one method which yield fault lengths on the order of 350km to 650km (e.g. Ji, 2004; Yagi, 2005). Another traditional method to delineate earthquake fault zones is plotting the aftershocks which occur in the first 24 hours following the main shock. The aftershocks are expected to cluster within the slip zone. This approach leads to an estimate of 1200km for the fault length (NEIC, 2004). In this study, the fault extent is constrained by observed tsunami travel times to the northwest, east, and south of the slip zone. Figure 3 displays the tsunami arrival time constraints on the fault zone. Tsunami arrival times at Paradip-India (SOI, 2005), Ko Tarutao-Thailand (Iwasaki, 2005), and Cocos Island (Merrifield et al., 2005) tide gages are plotted in reverse. That is, the observed travel time contour is plotted with the tide gage location as the origin point. This method indicates a fault zone approximately 1000km by 200km. The epicenter location lies on the southern end of the fault zone.

To accommodate trench curvature, the fault plane is broken into two segments. Fault parameters for the two segments are listed in Table 1. Strike, dip, and slip are based on the

definitions from Aki and Richards (1980). Strike is determined by the trench orientation. Dip is taken from the Harvard CMT solution (HRV, 2005). The slip for the southern segment is based on the Harvard CMT solution while slip for the northern segment is set at 90° based on observed tsunami first motions on Indian tide gages (NIO, 2005). Depth is based on the finite fault inversion of Ji (2004). The total moment release (derived by assuming an average slip of 13m and rigidity of 4.2×10^{11}dyne cm^{-2}) in the two segments equals 1.08×10^{30} dyne cm (Mw=9.3) which is in good agreement to 1.3×10^{30} dyne cm proposed by Stein and Okal (2005) based on normal mode analysis.

Table 1. Fault parameters used to generate vertical sea floor movement.

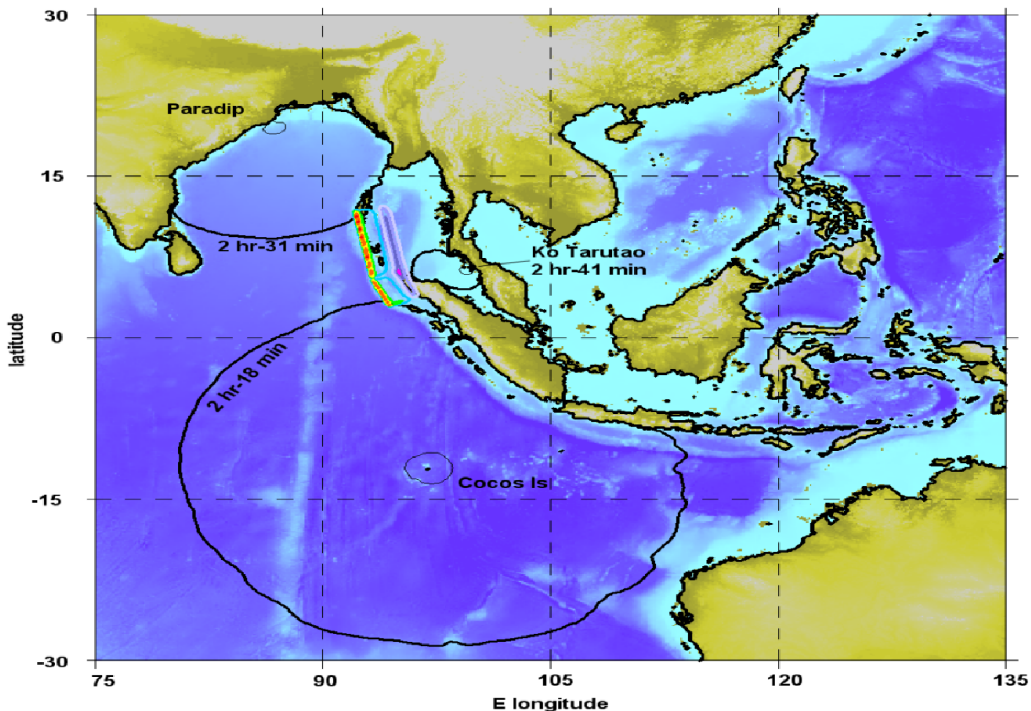| Earthquake Parameter	Southern Fault Segment	Northern Fault Segment
Strike	335°	350°
Dip	8°	8°
Slip	110°	90°
Length	300 km	700 km
Depth (SW corner)	8 km	8 km
SW corner Latitude	3.0N	5.6N
SW corner Longitude	94.4E	93.3E
Moment	3.2×10^{29}dyne cm	7.6×10^{29}dyne cm
Rigidity	4.2×10^{11}dyne cm^{-2}	4.2×10^{11}dyne cm^{-2}

Figure 3. December 26, 2004 Sumatra earthquake uplift as constrained by tsunami travel times.

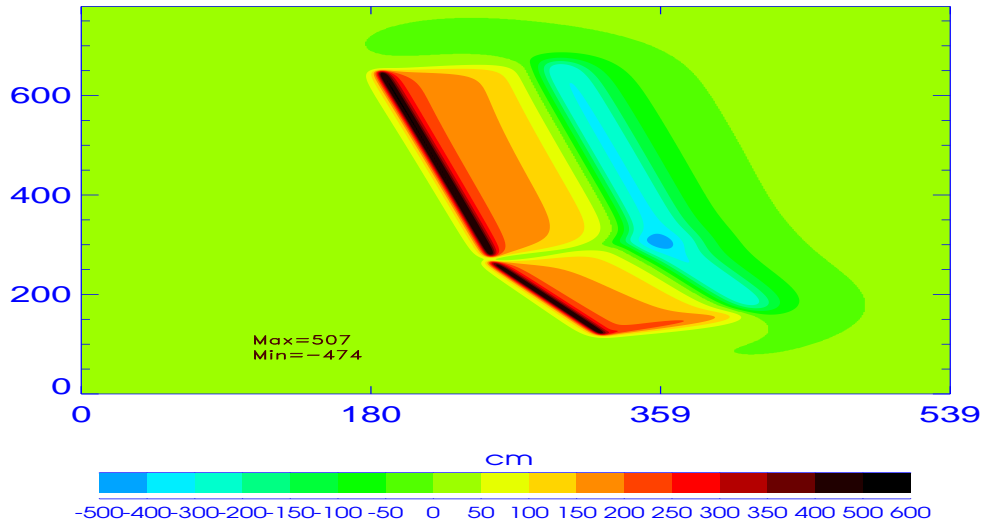The contours of the source functions are given in Fig.4.

Figure 4. The source deformation contours. Maximum uplift is 507 cm and maximum subsidence approximately 474 cm. Coordinates are given in geographical minutes. Point (0,0) is located at 89°E and 1°N.

The total potential energy related to the bottom deformation given in Fig. 4 which is transferred to the sea level oscillations is calculated as

$$E_p = 0.5 \int \int \rho g \zeta^2 R_\circ^2 \delta\phi\delta\lambda$$

Calculation over the area of deformation sets the potential energy to 5.39×10^3TJ (terra joule).

4. Global distribution of maximum amplitude.

Model computations using the above source were made for the 50 hrs of propagation so that the tsunami signal could travel over the entire World Ocean. During this computation the maximum tsunami amplitude in every grid point was recorded. The plot of maximum amplitude in the proximity of the generation domain is given in Figure 5 and the corresponding plot for the World Ocean is given in Figure 6. The strongly directional signal generated by the elongated source dominates the Indian Ocean domain. The main energy lobe is directed towards Sri Lanka and the secondary lobe points towards South Africa, sending a strong signal into the Atlantic Ocean. The maximum amplitude is 15.5m in proximity to the fault, 9.3 m at the shore of Thailand, 8.1 m at Sri Lanka, and 3.3 m at the coast of East Africa.
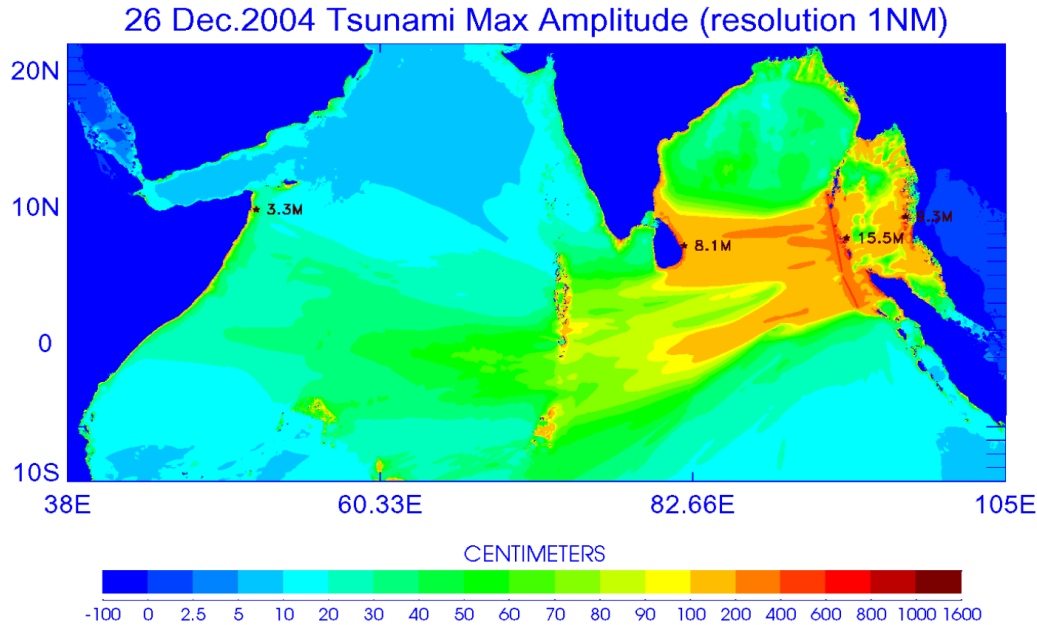
Figure 5. Maximum amplitude in the Indian Ocean.

This figure also depicts the amplitude enhancement in the shallow water and especially in proximity to peninsulas and islands due to energy concentration through the refraction process. The large domain of the Arabian Sea is located in the shadow of the main energy beam. Both computation and observation demonstrate significant increase of the tsunami amplitude up to 1.5 m at the coast of Oman at tide gauge in Salalah.

This global maximum amplitude distribution (Figure 6) shows that the Indonesian tsunami traveled all over the World Ocean. Although the source directivity pushed most of the wave energy towards South Africa, nonetheless quite a strong signal is directed towards the Antarctica. It is easy to see by checking the bathymetry that tsunamis tend to propagate towards Antarctica along the oceanic ridges and subsequently continues to transfer higher energy along the South Pacific ridge towards South and Central America. This mode of propagation brings the tsunami amplitude up to 65cm along the Pacific coast of South America. A similar mode of energy transfer is observed in the Atlantic, where the Mid-Atlantic Ridge channels the tsunami to produce 30cm wave amplitude as far north as Nova Scotia. An especially large energy flux is ducted from the South Atlantic Ridge towards Brazil and Argentina. The filaments of energy trapped along the South Pacific Ridges are most spectacular as they duct tsunami energy for many thousands of kilometers. A simple explanation of the energy trapping using the continuity equation leads us to conclusion that the amplitude should increase over the ridges due to shallower depth. At the same time the role of the bottom friction over the 2km deep ridge is negligible and therefore the tsunami can travel long distance without energy losses.
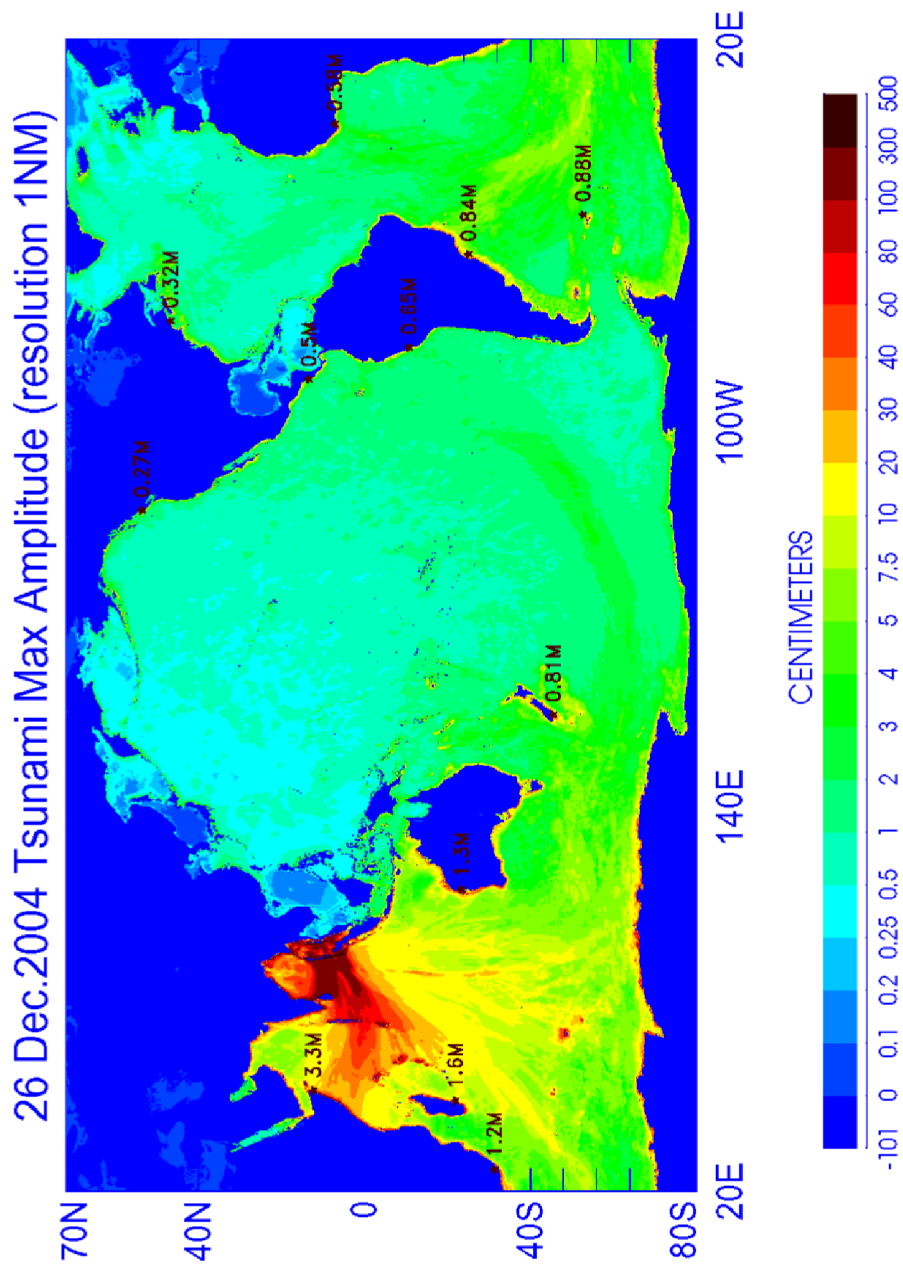
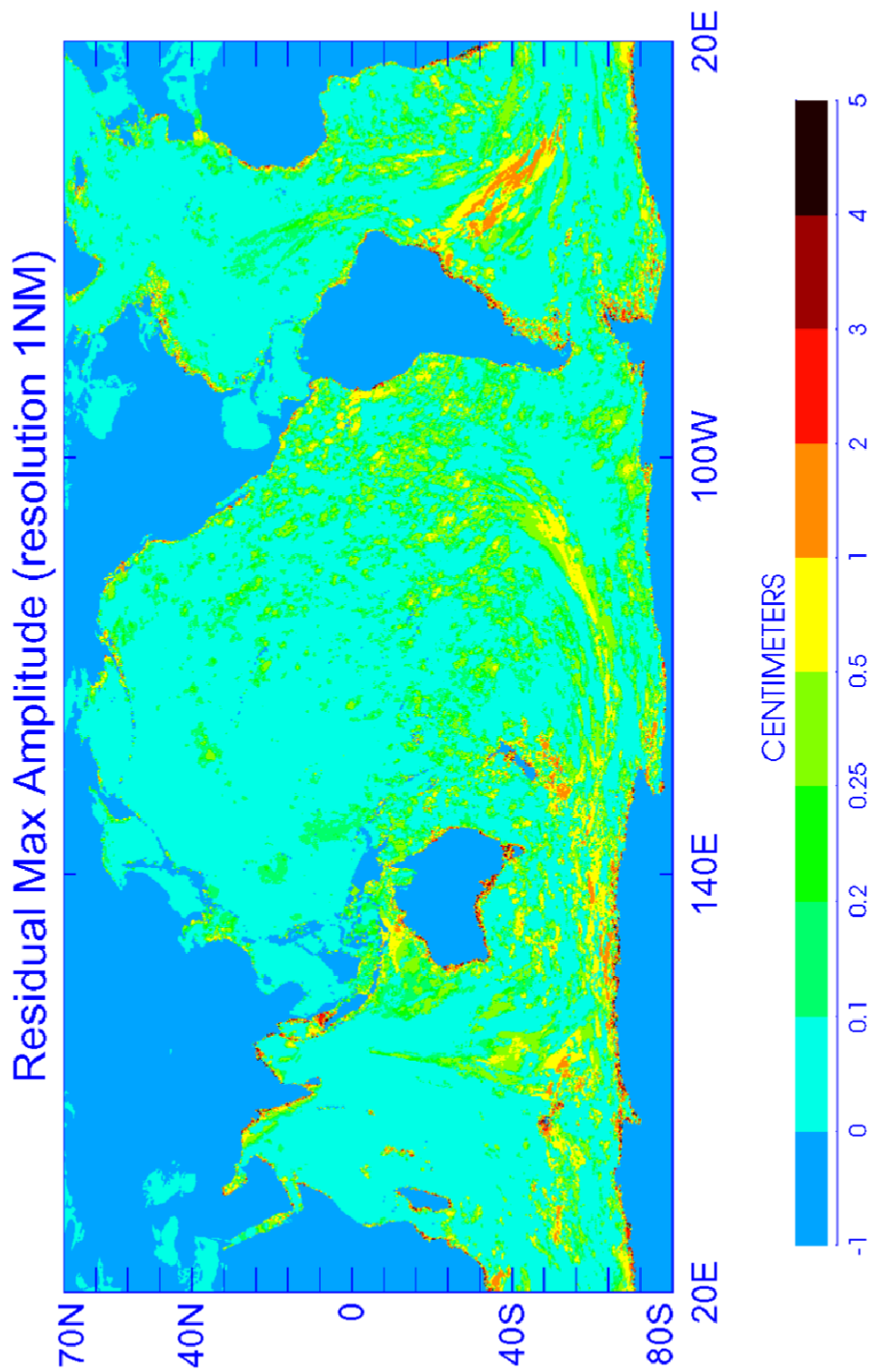**Figure 6.** Maximum amplitude in World Ocean.

Figure 7. Residual maximum amplitude in World Ocean.

The trapping of this energy is probably related to the long waves trapped along the ridge (Mei, 1989). The cross-ridge trapping length, which is responsible for energy concentration, is approximately defined by the tsunami wavelength. As the Indonesian tsunami carried a wide spectrum of waves with periods from 20 to 50min, the wavelength for the mid-ocean travel is in the range of 100km to 600km. A simple explanatory model for the long wave trapping may be based on different speed of the tsunami wave over and off ridge. As the wave over ridge is slower and wave off ridge is faster, the joint tsunami wave front is curved in such a way that the energy is fluxed towards the ridge.

The above explanation neglects the influence of the Coriolis force on tsunami propagation. Tsunamis are typically computed without Coriolis force because their periods are much smaller than the inertial period. As propagation proceeds over long distances the compounding effect of Coriolis force may sum up and increase. In Fig. 7 the residual maximum amplitude is given as difference between two computed distribution, with and without Coriolis force. The difference given in Fig. 7 shows locations where Coriolis force dominates. The amplitudes are not very large and according to expectation the influence is increasing towards the south since the Coriolis term increase poleward from equator. Consistent change is observed along the South Pacific Oceanic Ridge. Residuals due to Coriolis force are close to 1cm and since the total amplitude along this ridge according to Fig. 6 is approximately 4cm, we may conclude that Coriolis force plays a certain role in the energy trapping along the oceanic ridges (see also trapping in the South Atlantic). A simple model for energy trapping due to the Coriolis force is a Kelvin wave propagating along the depth discontinuity (Longuet-Higgins, 1969). The across-discontinuity trapping distance is defined by the Rossby radius of deformation (Gill, 1982). This distance is a function of depth and latitude and for the depth from 1km to 4km and for latitude of 40° to 60° the Rossby radius ranges from 1000km to 2000km. As this length is much larger than the tsunami wavelength we can conclude that Coriolis force is less effective in the concentrating tsunami energy along the oceanic ridges.

5. Travel time.

Tsunami travel time from the source region to the given location is important parameter in the tsunami prediction and warning. The Indonesian tsunami arrival times have been determined for many locations (Merrifield et al,2005; Rabinovich, 2005; http://www-sci.pac.dfo-mpo.gc.ca/osap/projects/tsunami/tsunamiasiax_e.htm; http://ilikai.soest.hawaii.edu/uhslc/iotd/; http://www.nio.org/jsp/tsunami.jsp). This set of data presents a possibility for the ocean-wide comparison of the data and the model. The first numerical experiment delineates the tsunami arrival time at every grid points for a signal of 0.1cm amplitude. The computed tsunami travel time chart is depicted in Fig. 8. The chart shows that even at such small limiting amplitudes the tsunami signal arriving at Alaska and North America did not pass through the Indonesian Straits but rather around the Australia and New Zealand.

The next numerical experiment computes isolines of arrival time for the tsunami signal of 0.5cm amplitude (Figure 9). In the vast regions of Northern and Central Pacific this figure does not show a consistent arrival time. We may conclude that the main premise used to construct these figures, namely that the first train of tsunami waves is associated
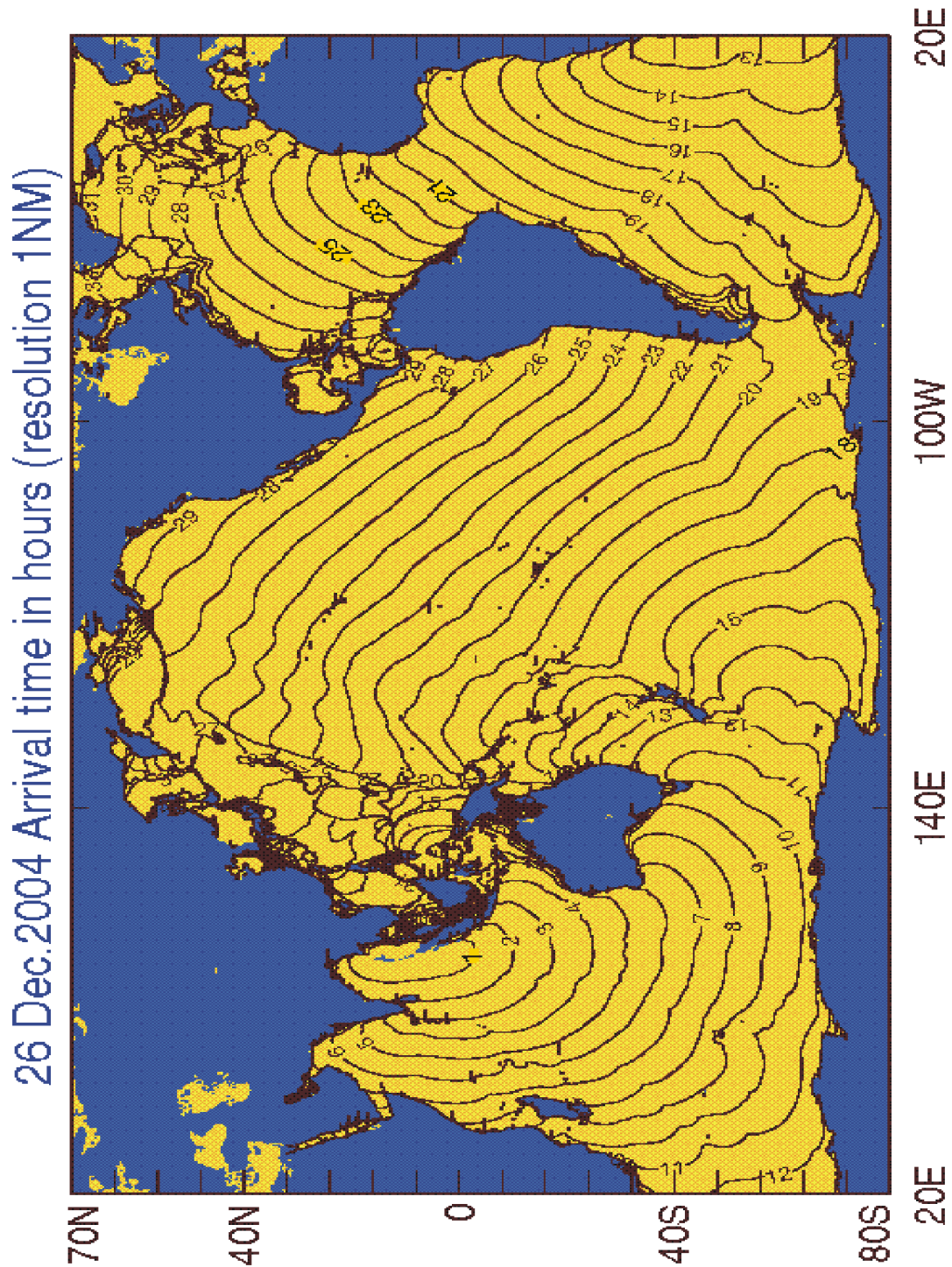
with the largest wave, does not hold true.

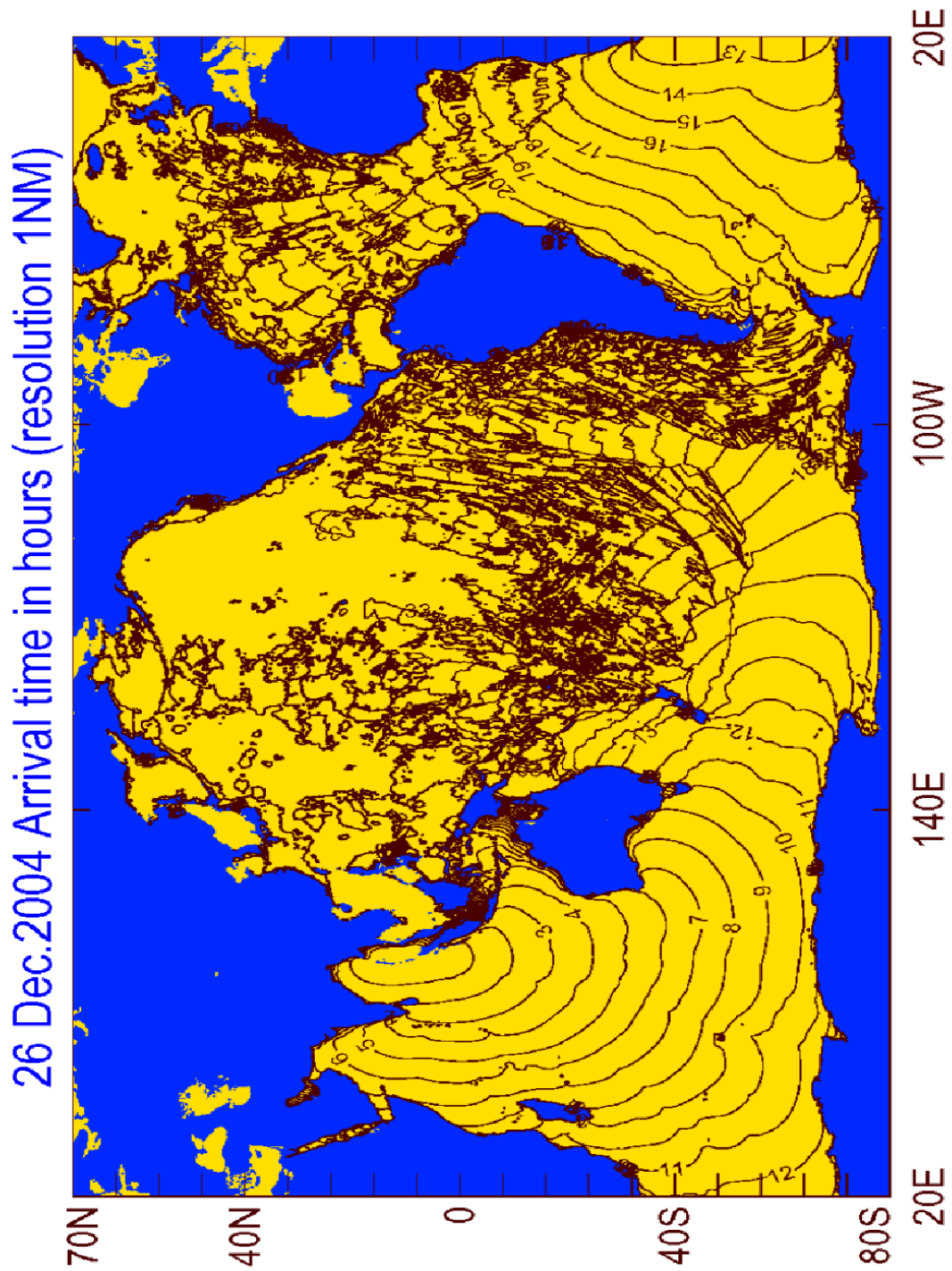**Figure 8. Travel time (in hours) for the tsunami of 0.1cm amplitude.**

Figure 9. Travel time (in hours) for the tsunami of 0.5cm amplitude.

Science of Tsunami Hazards, Vol. 23, No. 1, page 53(2005)

We were able to construct isolines in the regions of larger amplitudes, i.e. in Indian Ocean, in South Pacific (especially along the South Pacific Ridge) and in South Atlantic. By checking results of computation at the coastal locations it is easy to see that the tsunami of 0.5cm amplitude arrived at every location in the Pacific Ocean. This wave did not arrived at western North America by refracting around New Zealand; it traveled closer to South America via energy ducts located over South Pacific ridges. This is quite a long travel time as compared to the travel time depicted in Fig. 8.

In Table 2., the observed arrival time is compared with the computed arrival time of 0.1cm and 5cm tsunami amplitude. The observations define travel times uniquely when amplitude of the signal is above the noise level. The mixed signal of meteorological and tsunami origin is difficult to differentiate. We took, somewhat arbitrarily, the amplitude of 5cm as a signal strong enough to be seen above the meteorological noise. As can be seen from Figs. 8 and 9 in many locations, and as close to the source as New Zealand, the first waves to arrive were quite small and they slowly increased in amplitude. For example, the observed arrival time for the Jackson Bay, NZ is 18h18min while according to the sea level computed at 0.1cm at this location the arrival time for the first wave was 12h30min.

Table 2. Observed and calculated travel time.

Station location	Travel time observed	Travel time for 0.1cm amplitude	Travel time for 5cm amplitude
Chennai, (80°.17E, 13°.04N	2h36min	2h18min	2h20min
Male, (73°.52E, 4°.18N	3h25min	3h12min	3h18min
Hanimadhoo, (73°.17E, 6°.77N)	3h41min	3h24min	3h30min
Diego Garcia, (72°.40E, 7°.28S)	3h55min	3h40min	3h40min
Hillarys, (115°.73E, 31°.82S)	6h41min	6h24min	6h36min
Salalah, (54°.00E, 16°.93N)	7h17min	7h6min	7h6min
Pt. La Rue, (55°.53E, 4°.57S)	7h25min	7h24min	7h24min
Lamu, (40°.90E, 2°.27S)	9h9min	8h30min	8h30min
Zanzibar, (39°.18E, 6°.15S)	9h49min	10h24min	10h36min
Portland, (141°.60E, 38°.33S)	10h39min	9h48min	10h18min
Richard's Bay, (32°.08E, 28°.80S)	11h13min	11h00min	11h12min
Port Elizabeth, (25°.63E, 33°.97S)	12h28min	12h00min	12h6min
Jackson Bay, (168°.62E, 43°.98S)	18h18min	12h30min	19h30min
Arraial de Cabo, (42°.02W, 22°.97S)	21h56min	20h54min	21h30min
Arica, (70°.21W, 18°.22S)	26h36min	26h6min	29h20min
Char. Amalie,(64°.55W, 18°.20N)	28h42min	27h45min	33h30min
San Diego, (117°.12W, 32°.45N)	31h25min	29h0min	35h30min
Halifax, (63°.59W, 44°.66N)	31h30min	30h6min	32h6min
Atl.City,(74°.25W, 39°.21N)	31h48min	30h45min	33h30min
Toffino, (125°.55W, 49°.09N)	32h1min	29h0min	38h30min
Adak, (176°.65W, 51°.87N)	35h	27h	40h

In the Pacific Ocean the stations located in the Northern Pacific show the large dif-

ferences between the calculated and observed travel time. This is caused either by small tsunami signal to noise ratio or by multiple paths between the source and gauge locations. In the latter, especially important is an interaction of the higher energy tsunami signals which travel slowly over the oceanic ridges and the lower energy signals which travel faster over the deep oceanic regions.

References

Aki, K. and P. G. Richards. 1980. Quantitative Seismology Theory and Methods Volume 2, W.H. Freeman and Co., 557 pp.

Flather, R.A. and Heaps, N.S. 1975. Tidal computations for Morecambe Bay. *Geophys. J. Royal Astr. Soc.*, **42**, 489-517.

Gill A. E. 1982. *Atmosphere-Ocean Dynamics*, Academic Press, 662 pp.

Goring D. 2005. Sumatra Tsunami at New Zealand Ports and Harbours, http://www.mulgor.co.nz/SumatraTsunami/index.htm.

HRV - Harvard CMT Catalog (2005). Harvard Seismology: Centroid-Moment Tensor Project, posted at http://www.seismology.harvard.edu/CMTsearch.html.

Imamura F. 1996. Review of tsunami simulation with a finite difference method. In *Long-Wave Runup Models*, H.Yeah, P. Liu and C. Synolakis, Eds, World Scientific, 25–42.

Iwasaki, S.I. (2005). Posting of Thailand tide gage data to Tsunami Bulletin Board, also posted at http://www.navy.mi.th/hydro/tsunami.htm.

Ji, C. (2004). Preliminary Result of the 04/12/26 (Mw 9.0), OFF W COAST of Northern Sumatra Earthquake, posted at
http://www.gps.caltech.edu/%7Ejichen/Earthquake/2004/aceh/aceh.html.

Kowalik, Z. 2003. Basic Relations Between Tsunami Calculation and Their Physics - II , *Science of Tsunami Hazards*, v. 21, No. 3, 154-173

Kowalik, Z. and Murty, T.S. 1993a. *Numerical Modeling of Ocean Dynamics*, World Scientific, 481 pp.

Kowalik, Z. and Murty, T.S. 1993b. Numerical simulation of two-dimensional tsunami runup. *Marine Geodesy*, 16, 87–100.

Longuet-Higgins, M. S. 1969. On the transport of mass by time-varying ocean currents, *Deep-Sea Res.*, 16, 431–447.

Mader, C. L. 2004. *Numerical Modeling of Water Waves*, CRC Press, 274 pp.

Mei, C. C. 1989. *The Applied Dynamics of Ocean Surface Waves,* World Scientific, 740 pp.

Merrifield, M.A., Y.L. Firing, G. Brundrit, R. Farre, B. Kilonsky, W. Knight, L. Kong, C. Magori, P. Manurung, W. Mitchell, F. Shillington, E.M.S. Wijeratne, J. Jardin, S. Nakahara, F.-Y. Porter, and N. Turesky (2005). Tide Gauge Observations of the Indian Ocean Tsunami, December 26, 2004, manuscript submitted to *Geophysical Research Letters* Jan., 2005.

NIO - India National Institute of Oceanography (2005). 26 December 2004 Tsunami, posted at http://www.nio.org/jsp/tsunami.jsp.

NEIC - U.S. National Earthquake Information Center (2004). Magnitude 9.0 OFF THE WEST COAST OF NORTHERN SUMATRA Sunday, December 26, 2004 at 00:58:53 UTC Preliminary Earthquake Report, posted at http://neic.usgs.gov/neis/bulletin/neic_slav_ts.html

Okada, Y. (1985). Surface deformation due to shear and tensile faults in a half-space, *Bulletin of the Seismological Society of America*, 75, 1135-1154.

Rabinovich, A.B. 2005. Web compilation of tsunami amplitudes and arrival times. http://www-sci.pac.dfo-mpo.gc.ca/osap/projects/tsunami/tsunamiasia_e.htm.

Reid, R.O. and R.O. Bodine. 1968. Numerical model for storm surges in Galveston Bay. *J. Waterway Harbour Div.*, 94(WWI), 33–57.
SOI - Survey of India (2005). Preliminary report of tsunami observations, posted at http://www.surveyofindia.gov.in/tsunami4.htm.

Stein, S. and Okal E. (2005). Ultra-long period seismic moment of the great December 26, 2004 Sumatra earthquake and implications for the slip process, posted at http://www.earth.northwestern.edu/people/seth/research/sumatra2.html.

Yagi, Y. (2005). Preliminary Results of Rupture Process for 2004 OFF COAST OF NORTHERN SUMATRA Giant Earthqauke (ver. 1), posted at http://iisee.kenken.go.jp/staff/yagi/eq/Sumatra2004/Sumatra2004.html.